Hybrid Circuits with Nanofluidic Diodes and Load Capacitors: Experimental and Theoretical Studies

P. Ramirez,[1,*] V. Garcia-Morales,[1] V. Gomez,[1] M. Ali,[2,3] S. Nasir,[3] W. Ensinger,[2,3] and S. Mafe[4]

[1]*Dept. de Física Aplicada, Universitat Politècnica de València, E-46022 València, Spain*
[2]*Dept. of Material- and Geo-Sciences, Materials Analysis, Technische Universität Darmstadt, D-64287 Darmstadt, Germany*
[3]*Materials Research Department, GSI Helmholtzzentrum für Schwerionenforschung, D-64291 Darmstadt, Germany*
[4]*Dept. de Física de la Tierra i Termodinàmica, Universitat de València, E-46100 Burjassot, Spain*

The chemical and physical input signals characteristic of micro- and nanofluidic devices operating in ionic solutions should eventually be translated into output electric currents and potentials that are monitored with solid-state components. This crucial step requires the design of hybrid circuits showing robust electrical coupling between ionic solutions and electronic elements. We have studied experimentally and theoretically the connectivity of the nanofluidic diodes in single pore and multipore membranes with conventional capacitor systems for the cases of constant, periodic, and white noise input potentials. The experiments demonstrate the reliable operation of these hybrid circuits over a wide range of membrane resistances, electrical capacitances, and solution pH values. The model simulations are based on phenomenological equations that provide a convenient description of the electrical circuit operation. The results should contribute to advance signal transduction and processing using nanopore-based biosensors and bioelectronic interfaces.

I. INTRODUCTION

Micro and nanofluidic devices operating in ionic solutions allow a wide range of functionalities because of the different pore surface functionalizations currently available [1–4]. The interaction between the ions and the specific molecules functionalized on the pore surface of these soft nanostructures can be externally modulated by means of thermal, chemical, electrical and optical signals [1–4]. The different nature of these input signals is crucial in applications such as electrochemical energy conversion, logic responses in sensors and actuators, and signal processing in bioelectrical interfaces [1,5–7]. However, to achieve full functionality, the physical responses at the nanoscale should eventually be translated into electric current and potential signals that are monitored with solid-state components. Therefore, significant physical advances require an efficient electrical coupling between the nanofluidic devices and conventional electronic elements such as capacitors in hybrid circuits.

We have studied recently the conversion of white noise, zero average electrical potentials into net currents by using single nanofluidic diodes [8] and protein ion channels [9]. To check further the connectivity between these liquid-state nanostructures and conventional capacitor systems, we propose now to study experimentally and theoretically some fundamental theorems concerning energy conversion and charge transfer in hybrid networks.

The experimental results concern single pore and multipore membranes and show the reliable operation of circuits where different load capacitors are interconnected with soft nanostructures that act as potential-dependent resistances. The phenomenological equations for the current-voltage curves of the nanofluidic diodes allow the analysis of hybrid circuits similarly as in the case of conventional solid state circuits. For the sake of generality, we use constant, periodic, and white noise input potential signals. The membrane resistances are between 1 kΩ and 1 GΩ, and the capacitances of the load capacitors vary between 10 nF and 10 mF. The electrolyte solution properties cover a wide range of pH values between 1 and 7, approximately. Because of the wide

range of physical and chemical conditions considered, the experimental and theoretical results should contribute to advance signal transduction and processing using nanopore-based biosensors and bioelectronic interfaces [1,5,7–10].

II. EXPERIMENTAL METHODS

A. Nanofluidic diode fabrication

We used membrane samples with 1 and 10^4 tracks per cm^2 obtained from stacks of 12.5-μm thick polyimide (PI) foils (Kapton50 HN, DuPont) that were irradiated with swift heavy ions (Au) of energy 11.4 MeV per nucleon under normal incidence at the linear accelerator UNILAC (GSI, Darmstadt). Under these conditions, the range of heavy ions in PI was larger than the thickness of the six foil stack so that the energy loss of the ions was above the threshold required for homogeneous track etching. In front of each stack, a metal mask with a 200 μm diameter centered aperture was placed for the case of single-ion irradiation. As soon as a single ion passed through the foil stack and registered by a particle detector behind the samples, the ion beam was blocked. The procedure gave tracks in the membrane that were converted into approximately conical pores by asymmetric track-etching techniques [11,12]. The track-etching processes yielded carboxylate residues on the pore surface that eventually result in fixed charges when the membrane is exposed to aqueous ionic solutions of KCl and different pH values. The sign of these charges depends on the solution pH and the approximately conical pore geometry is responsible for the electrical rectification characteristic of the nanofluidic diodes [11,12].

B. Electrical measurements

Figure 1(a) shows a scheme of the hybrid circuit. The picoammeter/voltage source (Keithley 6487/E) provides the input potential $\varepsilon(t)$ and controls the current I through the circuit obtained upon closing the switch at time $t = 0$. The potential drops across the nanofluidic diode (V_D) and the load capacitor (V_C) of capacitance C are measured with a multimeter (Keithley 2000/E).

Figure 1(b) shows a scheme of the electrochemical cell with the nanofluidic diode for the single pore membrane case. The membrane area exposed to the aqueous ionic solutions was 1 cm^2. The membrane samples were bathed by 0.1 M KCl electrolyte solutions under controled pH conditions. Ag|AgCl electrodes immersed in the bathing solutions were employed to introduce the input potentials in the electrochemical cell and measure the electric currents. Note the sign criteria used for voltages and currents.

Figures 1(c) and 1(d) show the typical current-voltage ($I-V_D$) curves obtained for the single pore and multipore membranes, respectively. These curves could be described by using the phenomenological model of the *Appendix* and the pore parameters shown in the insets of Figs. 1(c) and 1(d). Low pore resistances R_+ were observed when the current entered the cone tip, while high resistances R_- were obtained when the current entered the cone base [8]. The reproducibility of the nanopore $I-V_D$ curves and the membrane responses was checked several times in all experiments conducted with the different circuits. From the steady-state $I-V_D$ curves, pore radii in the ranges 10−40 nm (cone tip) and 300−600 nm (cone base) were obtained [12].

II. RESULTS AND DISCUSSION

Figures 2(a) and 2(b) schematically show the charging (time $t = 0$) and discharging (time $t = t_s$) circuits for two nanofluidic diode configurations together with the experimental curves obtained at the constant input potential $\varepsilon = 2$ V for single pore (Figs. 2(c) and 2(d)) and multipore (Figs. 2(e) and 2(f)) membranes. In Figs. 2(c) and 2(e), the charging of capacitor 1 proceeds through the nanodiode high-conductive polarity, while the charge transfer to capacitor 2 occurs through the low-conductive polarity. The opposite case is considered in Figs. 2(d) and 2(f). As in the conventional resistor-capacitor circuit (RC circuit), the capacitor voltage V_{C1} eventually reaches the source voltage. Upon the discharge to capacitor 2, half of the energy initially stored in capacitor 1 is finally stored in capacitor 2, regardless of the particular

nanodiode resistance characteristic of the charge transfer process. The time constants of the RC circuits of Figs. 2(a) and 2(b) are shown in Table I for the charging experiments of Figs. 2(c)–2(f). For the charge transfer, the final voltage of capacitors is $V_{st} = C_1V/(C_1 + C_2)$ and then the dissipated energy is $(1/2)\varepsilon^2 C_1 C_2/(C_1 + C_2)$ regardless of the particular nanodiode resistance characteristic of the process. The time constants of the RC circuits of Figs. 2(a) and 2(b) are shown in Table II for the charge transfer experiments of Figs. 2(c)–2(f). Note the excellent agreement between the theoretical steady state voltages V_{st} and the experimental saturation voltages of Figs. 2(c)–2(f). This is also the case of the theoretical and experimental time constants.

Figure 3(a) considers the case of a periodic input signal of zero average and the multipore membrane for the charging circuit of Fig. 1(a). The sinusoidal signal of amplitude of 2 V has a period of 105 s. Because of the electrical rectification, the capacitor is charged with time. For high enough capacitances, the oscillating capacitor voltage attains an average value which is independent of the capacitance. On the contrary, the charging time constant increases with this capacitance, while the oscillation amplitude decreases with the capacitance (see *Appendix*). Figure 3(b) shows the $I-\varepsilon$ curve for the circuit of Fig. 1(a). The experimental loop gives the minimum and maximum values of the capacitor voltage V_C defined by the condition of zero current, $I = 0$. The curves obtained with the theoretical model of the *Appendix* are in good agreement with the experimental results (see Figs. 3(c) and 3(d)).

Figure 4 shows the case of the white noise input signal for single pore (Figs. 4(a) and 4(b)) and multipore (Figs. 4(c) and 4(d)) membranes. This case is of interest for energy transduction using external noisy signals [8,9]. As observed previously, the limiting value of the capacitor voltage does not change with the capacitance (see Figs. 4(a)–4(c)), which is not the case of the time constants and the fluctuating potential amplitudes around the average potential. We have provided a theoretical justification of this experimental fact in the *Appendix*. The theoretical

results of Fig. 4(b) reproduce the observed behavior. Figure 4(d) shows the I–ε curve for the circuit of Fig. 1(a) in the case of the multipore membrane. The minimum and maximum values of the capacitor voltage V_C are now approximately described by the condition of zero current, $I = 0$. The amplitude between the extreme values of Fig. 4(d) approximately corresponds to the difference between the minimum and maximum fluctuating potentials of Fig. 4(c).

Figure 5 considers the effect of the solution properties (pH) on the I–V_D curves (Fig. 5(a)), the charging process (Figs. 5(b) and 5(c)), and the dependence of the steady state voltage V_{st} on the rectification ratio r (Fig. 5(d)). Note the effect of the pore fixed charge sign on the I–V_D curves: decreasing the pH causes a decrease in the negative surface charge density and eventually reverses it to give a positive charge density [12,13]. This experimental fact changes the sign of the voltage V_C in Figs. 5(b) (experiment) and 5(c) (model). The theoretical line of Fig. 5(d) is given by $V_{st} = (V_0/2)[(r-1)/(1+r)]$, as shown in the *Appendix*. Table III gives the different membrane resistances obtained from Fig. 5(a) as a function of the solution pH.

III. CONCLUSIONS

Fluidic devices operating in ionic solutions can be used to process a variety of chemical and physical signals. Input signals defined at the micro and nanoscale should eventually be translated into electric currents and potentials that are monitored with solid-state components [1,5–7]. This crucial step requires the design of circuits showing robust electrical coupling between the ionic solutions and the electronic elements. We have studied experimentally and theoretically the connectivity between liquid-state nanofluidic diodes and conventional capacitors. Fundamental questions concerning energy conversion and charge transfer in hybrid networks have been addressed. In particular, we have shown that the limiting value of the load capacitor voltage does not change with the capacitance for the different input signals used.

The experiments have been conducted using single pore and multipore membranes in the cases of constant, periodic, and white noise input potential signals. The extension of the analysis to single protein ion channels [9], and square wave and triangular signals [14,15] could also be possible. The membrane resistances, load capacitor capacitances, and solution pH values cover a wide range of experimental cases. The theoretical model is based on phenomenological equations that provide a good description of the electrical circuit operation.

APPENDIX

The theoretical model for the nanofluidic diode of Fig. 1 is based on a phenomenological equation for the current-voltage curve I–V_D:

$$I = \frac{R_+ V_D}{2r} \left[r + 1 + (r-1) \tanh\left(\frac{V_D}{V_T}\right) \right], \tag{A1}$$

where $r \equiv R_+ / R_-$ is the ratio of the resistances R_+ and R_- experimentally observed for high positive and negative voltages V_D, respectively. For high positive V_D, Eq. (A1) gives $I \approx R_+ V_D$ asymptotically while for high negative voltages V_D, it reduces to $I \approx R_- V_D$. Thus, the values of these resistances are obtained from independent experiments. The parameter V_T is the thermal voltage ($R_g T/F$) corrected by an empirical factor to give $V_T = 0.5$ V in our case, where R_g is the gas constant, T is the temperature, and F is the Faraday constant.

The time evolution of the potential V_C across the capacitor is governed by the equation $C dV_C / dt = I$, where I is the current of Eq. (A1). This differential equation can be discretized for small time steps Δt to give $V_{C,t+1} = V_{C,t} + \Delta t\, I/C$ where the second subscript makes reference to time. Since the voltage across the nanofluidic diode can be written as $V_D = \varepsilon - V_C$, we obtain

$$V_{C,t+\Delta t} = V_{C,t} + \Delta t \frac{\varepsilon - V_{C,t}}{\tau_{ch}} \left[1 + \frac{r-1}{r+1} \tanh\left(\frac{\varepsilon - V_{C,t}}{V_T}\right) \right], \tag{A2}$$

where we have introduced the characteristic time $\tau_{ch} \equiv (r+1)R_+ /(2rC)$. Eq. (A2) describes the

dynamics of the electric circuit in Fig. 1 and is used in the model results of Figs. 3–5. If the applied voltage ε is constant, the only fixed point of Eq. (A2) is $V_{st} = \varepsilon$ (a stable value).

We consider now the case of an applied voltage ε_t that takes random values in the interval $[-V_0, V_0]$ at each time step according to a uniform distribution. By introducing $t = n\Delta t$ with n a non-negative integer, we can obtain the time average of a generic magnitude f_t over a long time $T = N\Delta t$ as

$$\langle f_t \rangle = \frac{\Delta t}{T} \sum_{n=0}^{N-1} f_{n\Delta t}. \tag{A3}$$

Note that we have $\langle \varepsilon_t \rangle = 0$ because the applied voltage is uniformly distributed. When the capacitor potential has reached a stationary state, $\langle V_{C,t} \rangle = V_{st}$, with $\xi_t = V_{C,t} - V_{st}$ the deviation of the instantaneous capacitor potential from the average stationary state value, so that $\langle \xi_t \rangle = 0$. Therefore, we have from Eq. (A2) that

$$0 = \left\langle \Delta t \frac{\varepsilon_t - \xi_t - V_{st}}{\tau_{ch}} \left[1 + \frac{r-1}{r+1} \tanh\left(\frac{\varepsilon_t - \xi_t - V_{st}}{V_T} \right) \right] \right\rangle, \tag{A4}$$

and then

$$V_{st} = \frac{r-1}{r+1} \left\langle (\varepsilon_t - \xi_t - V_{st}) \tanh\left(\frac{\varepsilon_t - \xi_t - V_{st}}{V_T} \right) \right\rangle. \tag{A5}$$

In the limit $V_T \to 0$, we obtain

$$V_{st} = \frac{r-1}{r+1} \left\langle |\varepsilon_t - \xi_t - V_{st}| \right\rangle. \tag{A6}$$

For negligible small fluctuations $\xi_t \approx 0$, this equations reduces to

$$V_{st} = \frac{r-1}{r+1} \left\langle |\varepsilon_t - V_{st}| \right\rangle. \tag{A7}$$

The average $\langle x \rangle$ of a stochastic variable x uniformly distributed in the interval $[a, b]$ is $\langle x \rangle = (a+b)/2$ and then $\langle |\varepsilon_t - V_{st}| \rangle = V_0/2$ because $|\varepsilon_t - V_{st}|$ is uniformly distributed in the

interval $[V_0 - V_{st}, V_0 + V_{st}]$. Therefore, Eq. (A7) becomes

$$V_{st} = \left(\frac{r-1}{r+1}\right)\frac{V_0}{2},\tag{A8}$$

which shows that the average capacitor voltage depends linearly on the ratio $(r-1)/(r+1)$ and the maximum value V_0 of the applied voltage ε_t. This theoretical result is in good agreement with the experimental data of Fig. 5(d).

In addition, Eq. (A8) correctly predicts that the average stationary voltage does not depend on the capacitor characteristics, as shown in Fig. 4. However, the amplitude of the fluctuations does depend on the capacitance through the characteristic time τ_{ch}. Indeed, if we take $\xi_t = 0$ in Eq. (A2) for the stationary state, we obtain

$$\left|\xi_{t+\Delta t}\right| = \left|\Delta t \frac{\varepsilon_t - V_{st}}{\tau_{ch}}\left[1 + \frac{r-1}{r+1}\tanh\left(\frac{\varepsilon_t - V_{st}}{V_T}\right)\right]\right|,\tag{A9}$$

which reduces to

$$\left|\xi_{t+\Delta t}\right| = \frac{\Delta t}{\tau_{ch}}\left|\varepsilon_t - V_{st} + \frac{r-1}{r+1}\left|\varepsilon_t - V_{st}\right|\right|\tag{A10}$$

in the limit $V_T \to 0$. For $r \geq 1$, the maximum value $\left|\xi\right|_{\max}$ of any fluctuation around the stationary state can be obtained from Eq. (A10) with $\varepsilon_t = V_0$ and Eq. (A8) as

$$\left|\xi\right|_{\max} = \frac{\Delta t}{\tau_{ch}}\frac{r+3}{(r+1)^2}V_0.\tag{A11}$$

Eq. (A11) shows that low capacitances give high fluctuations around the average voltage. Note also that τ_{ch} is bounded below by Δt. If $r = 1$, $V_{st} = 0$ from Eq. (A8) and then $\left|\xi\right|_{\max} = \frac{\Delta t}{\tau_{ch}}V_0$ from Eq. (A11). Therefore, for small values of C, $\left|\xi\right|_{\max} \approx V_0$ and the signal becomes indistinguishable from the noisy applied voltage. This fact explains the results of Fig. 4 concerning the effect of capacitance on the observed fluctuations.

ACKNOWLEDGEMENTS

[1] M. Tagliazucchi and I. Szleifer, Transport mechanisms in nanopores and nanochannels: can we mimic nature? Mater. Today **18**, 131 (2015).

[2] Q. Liu, L. Wen, K. Xiao, H. Lu, Z. Zhang, G. Xie, X.-Y. Kong, Z. Bo, and L. Jiang, A biomimetic voltage-gated chloride nanochannel, Adv. Mater. **28**, 3181 (2016).

[3] P. Ramirez, J. Cervera, M. Ali, W. Ensinger, and S. Mafe, Logic functions with stimuli-responsive single nanopores, ChemElectroChem **1**, 698 (2014).

[4] G. Pérez-Mitta, A. G. Albesa, C. Trautmann, M. E. Toimil-Molares, and O. Azzaroni, Bioinspired integrated nanosystems based on solid-state nanopores: "*iontronic*" transduction of biological, chemical and physical stimuli, Chem. Sci. **8**, 890 (2017).

[5] N. Misra, J. A. Martinez, S.-C. J. Huang, Y. Wang, P. Stroeve, C. P. Grigoropoulos, and A. Noy, Bioelectronic silicon nanowire devices using functional membrane proteins, Proc. Natl. Acad. Sci. U.S.A. **106**, 13780 (2009).

[6] Y. Hou, R. Vidu, and P. Stroeve, Solar energy storage methods, Ind. Eng. Chem. Res. **50**, 8954 (2011).

[7] M. Ali, P. Ramirez, W. Ensinger, and S. Mafe, Information processing with a single multifunctional nanofluidic diode, Appl. Phys. Lett. **101**, 133108 (2012).

[8] V. Gomez, P. Ramirez, J. Cervera, S. Nasir, M. Ali, W. Ensinger, and S. Mafe, Charging a capacitor from an external fluctuating potential using a single conical nanopore, Sci. Rep. **5**, 9501 (2015).

[9] C. Verdia-Baguena, V. Gomez, J. Cervera; P. Ramirez, and S. Mafe, Energy transduction and signal averaging of fluctuating electric fields by a single protein ion channel, Phys. Chem. Chem. Phys. **19**, 292 (2017).

[10] O. Yehezkeli, R. Tel-Vered, J. Wasserman, A. Trifonov, D. Michaeli, R. Nechushtai, and I. Willner, Nat. Commun. **3**, 742 (2012).

[11] P. Apel, Track etching technique in membrane technology, Radiat. Meas. **34**, 559 (2001).

[12] M. Ali, P. Ramirez, S. Mafe, R. Neumann, and W. Ensinger, A pH-tunable nanofluidic diode with a broad range of rectifying properties, ACS Nano **3**, 603 (2009).

[13] J. Cervera, P. Ramirez, V. Gomez, S. Nasir, M. Ali, W. Ensinger, P. Stroeve, and S. Mafe, Multipore membranes with nanofluidic diodes allowing multifunctional rectification and logical responses, Appl. Phys. Lett. **108**, 253701 (2016).

[14] V. Gomez, P. Ramirez, J. Cervera, S. Nasir, M. Ali, W. Ensinger, and S. Mafe, Converting external potential fluctuations into nonzero time-average electric currents using a single

nanopore, Appl. Phys. Lett. **106**, 073701 (2015).

[15] E. Kalman, K. Healy, and Z. S. Siwy. Tuning ion current rectification in asymmetric nanopores by signal mixing, Europhys. Lett. **78**, 28002 (2007).
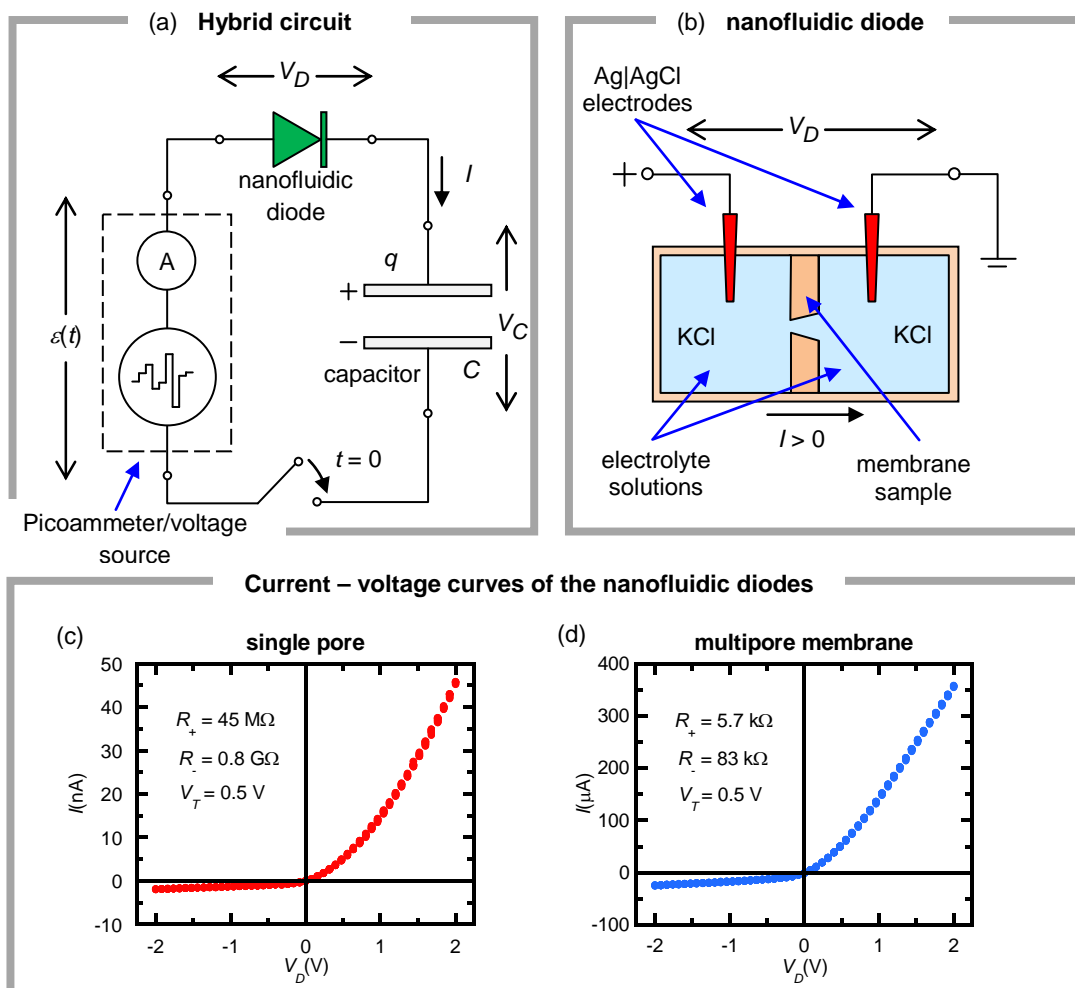
FIG. 1: The hybrid circuit with the nanofluidic diode and the load capacitor (a). The electrochemical cell with the nanofluidic diode (b). Typical current-voltage curves obtained for the single pore (c) and multipore (d) membranes obtained at pH = 6.6.
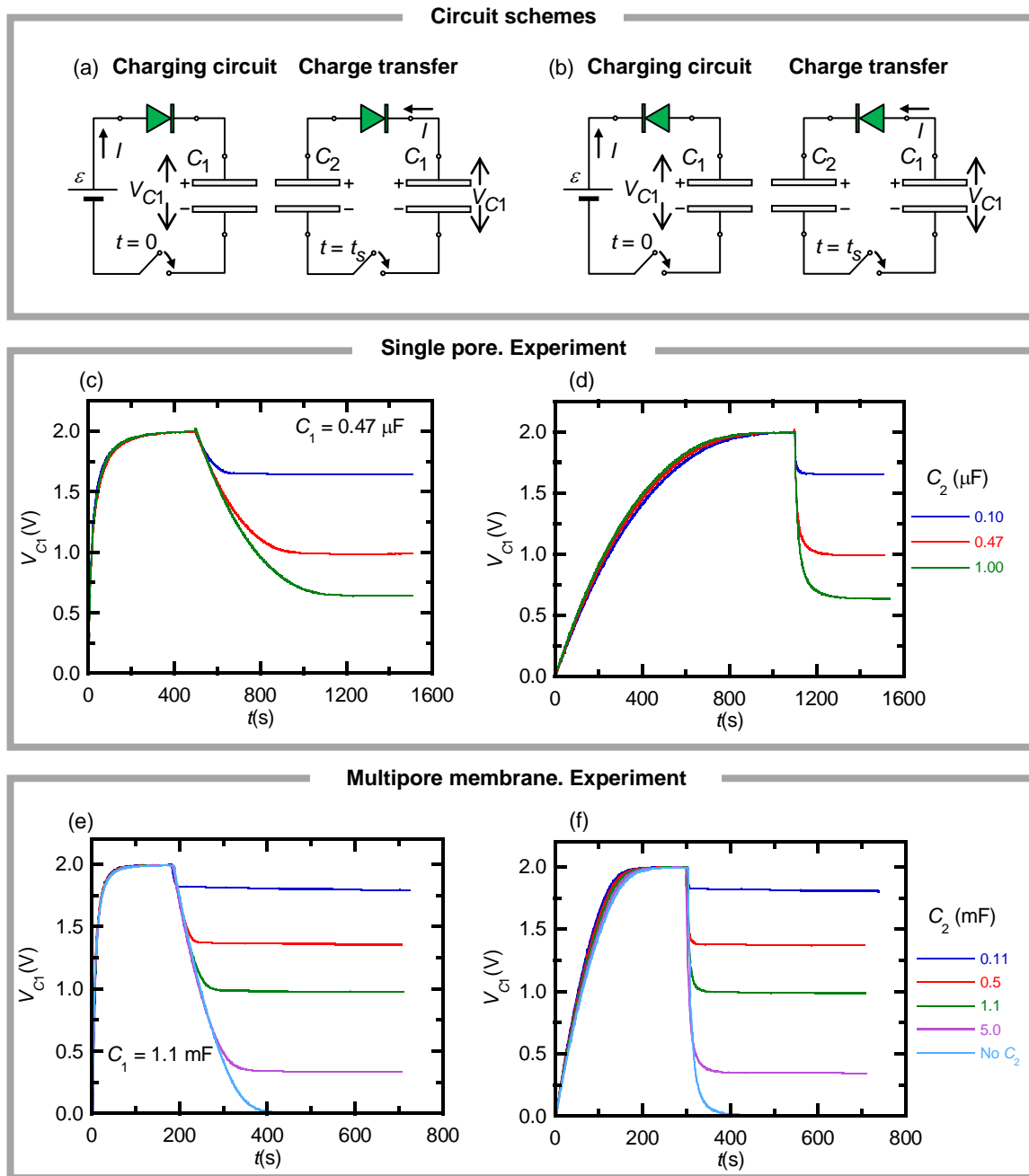
FIG. 2. The charging and discharging (charge transfer between capacitors) circuits for two nanofluidic diode configurations (a) and (b). Experimental curves measured for single pore membrane [(c) and (d)]. The curves correspond to $C_2 = 0.10$, 0.47, and 1.0 μF, from top to bottom. Experimental curves measured for multipore pore membrane [(e) and (f)]. The curves correspond to $C_2 = 0.11$, 0.5, 1.1, 5.0 and 0 mF, from top to bottom. All curves were obtained with constant input potential $\varepsilon = 2$ V.
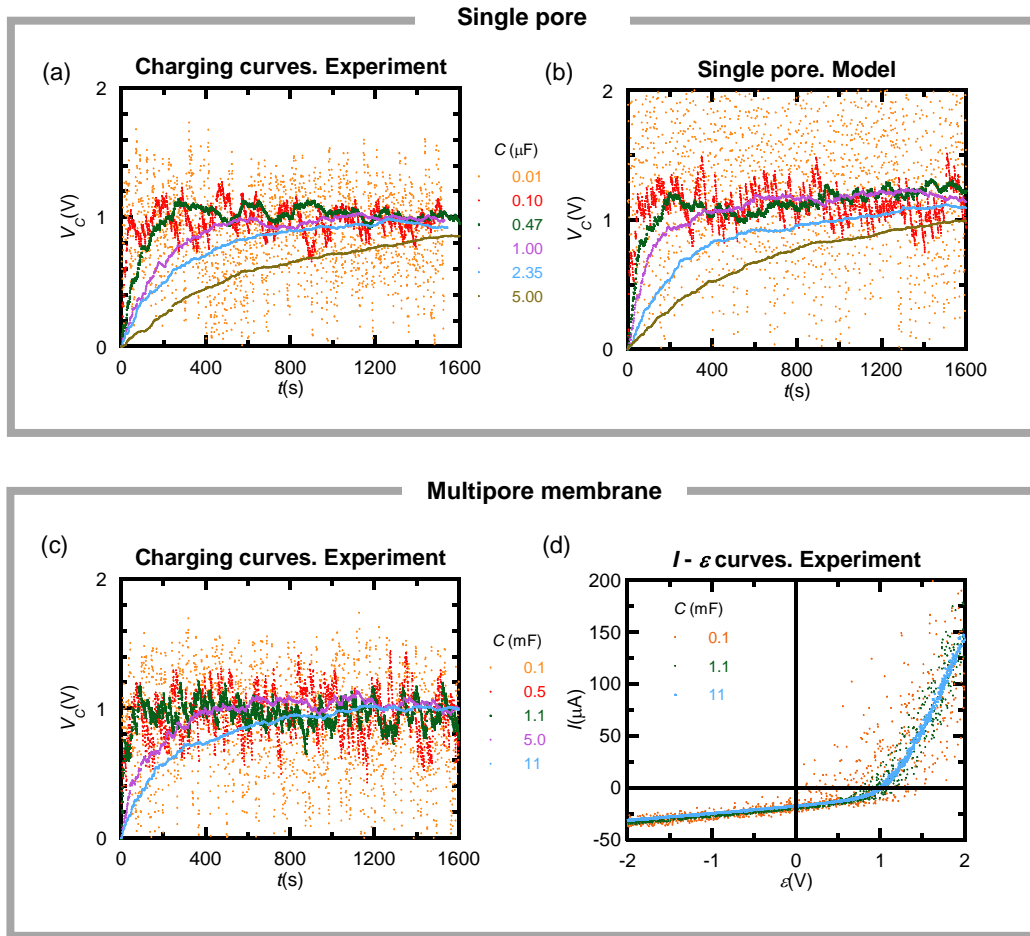
Sinusoidal input signal. Multipore membrane
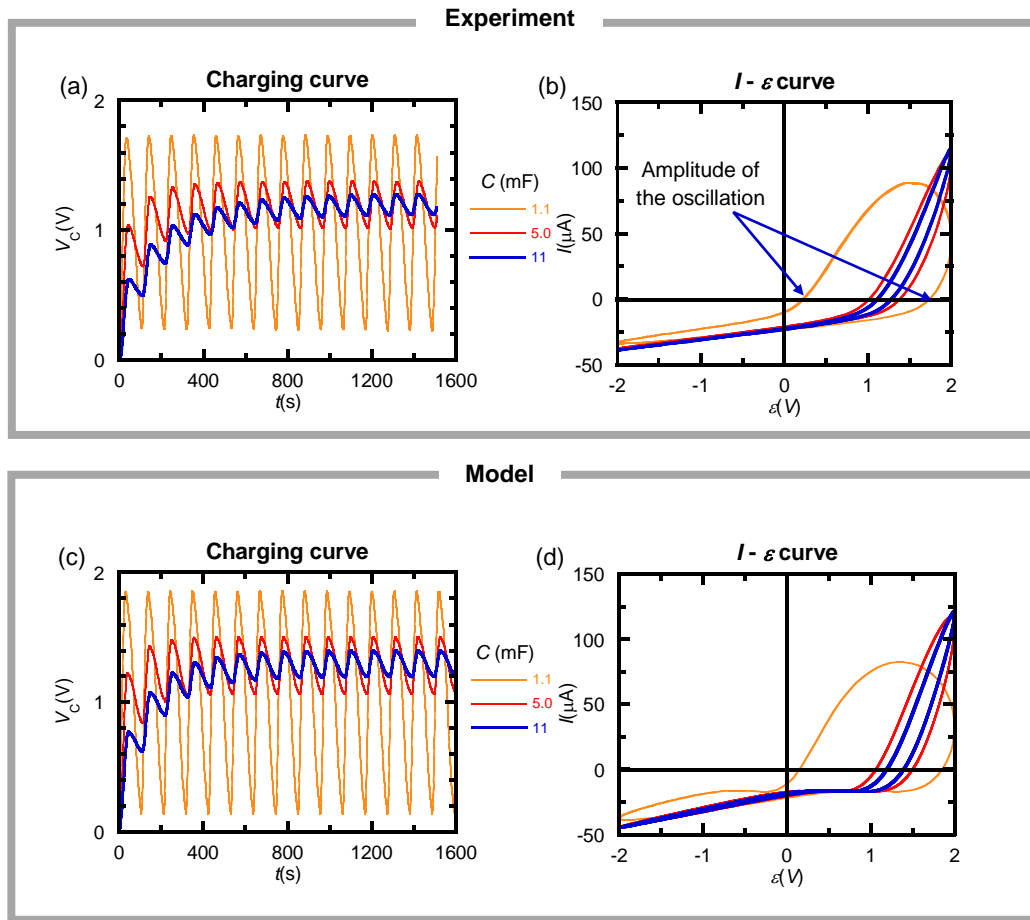
FIG. 3. Experiments with a periodic input signal (sinusoidal wave) of zero average and the multipore membrane [(a) and (b)]. Theoretical curves obtained with the model of the *Appendix* [(c) and (d)].
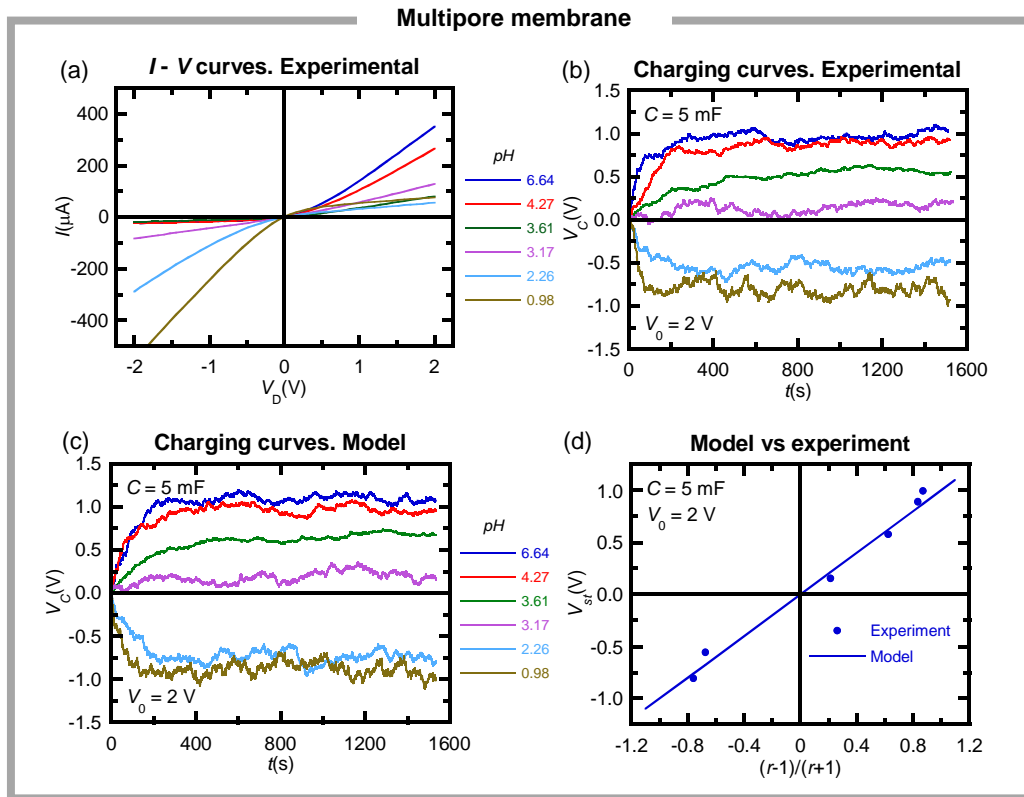
FIG. 4. Experiments with white noise input signals for single pore (a) and multipore membranes [(c) and (d)]. Theoretical results obtained with the model of the *Appendix* for the single pore (b). The most scattered data correspond to the lowest capacitance.

FIG. 5. Effect of the solution properties (pH) on the capacitor charging. Experimental current-voltage curves of the multipore membrane at different pH values and rectification ratios (a). Experimental charging curves of the capacitor at different pH values (b). Theoretical results obtained with the model of the *Appendix* (c). Dependence of the steady state voltage V_{st} on the rectification ratio r showing the agreement between the model of the *Appendix* and the experiments (d).

	Time constant (s)	
	Circuit (a)	Circuit (b)
Single pore	18	400
Multipore membrane	7	90

Table I: Time constants for the RC circuits of Figs. 2(a) and 2(b) in the charging experiments of Figs. 2(c)–2(f).

			Time constant (s)	
	C_2 (μF)	V_{st} (V)	Circuit (a)	Circuit (b)
Single pore	0.10	1.65	66	3.3
	0.47	1.00	188	9.4
	1.00	0.64	256	12.8
	C_2 (mF)	V_{st} (V)	Circuit (a)	Circuit (b)
Multipore membrane	0.11	1.82	8	0.6
	0.50	1.38	28	2.1
	1.10	1.00	44	3.3
	5.00	0.36	72	5.4
	No capacitor	0.00	88	6.6

Table II: Time constants, theoretical steady state voltages V_{st}, and capacitances of the RC circuits in Figs. 2(a) and 2(b) for the charge transfer experiments of Figs. 2(c)–2(f).

pH	$R_+(k\Omega)$	$R_-(k\Omega)$
6.64	5.7	83
4.27	7.5	82
3.61	25	107
3.17	24	16
2.26	36	7.0
0.98	27	3.6

Table III: Membrane resistances obtained from Fig. 5(a) as a function of the solution pH.